

packed along the *b* axis. Attempts to synthesize polar simple brick frameworks with related banana-shaped 1,3-benzene- and 2,4-dimethyl-1,5-benzenedisulfonates have failed. This most likely reflects excessive void space created by the absence of methyl substituents in key positions, including those projecting along the *b* axis (28).

A preliminary measurement of the SHG activity of these materials, using the Kurtz-Perry powder method (29), reveals that, as one would expect, the response scales according to the β values of the included guests. The highest SHG activity measured, in $G_2TMBDS \cdot (N,N\text{-dimethyl-4-nitroaniline})$, is 10 times that measured for potassium dihydrogen phosphate (KDP), an accepted SHG standard. G_2MDS (mesitylene) and G_2TMBDS (mesitylene), which contain a centric guest with no nonlinear optical activity, do not exhibit any measurable SHG response. Therefore, the polar host framework does not contribute significantly to the SHG activity, and the SHG activity is primarily associated with the polar guest arrays. This illustrates the fact that inclusion compounds can permit crystal architecture, provided by the host framework, to be separated from function introduced by the included guests, in this case SHG. The ionic GS host frameworks also bestow thermal stability (the inclusion compounds are stable to at least 180°C) on otherwise low-melting guests, an important consideration for nonlinear optics applications.

These results demonstrate that crystal engineering, using a protocol based on simple geometric principles, can include the prediction and control of lattice metrics and nominal space group symmetry. The ability to predict crystal structure with this level of detail is a rather unusual achievement in organic solid-state chemistry (30). Furthermore, this design produces a polar host framework from entirely achiral components, resulting in polar alignment of guest molecules that do not crystallize in polar space groups in their pure forms or that exist as liquids at room temperature. We anticipate that related frameworks constructed with pillars having significant hyperpolarizabilities also can produce materials with SHG activity.

References and Notes

1. P. Ball, *Nature* **281**, 648 (1996).
2. A. Gavezotti, *Acc. Chem. Res.* **27**, 309 (1994).
3. J. Maddox, *Nature* **201**, 335 (1988).
4. D. Y. Curtin, I. C. Paul, *Chem. Rev.* **81**, 525 (1981).
5. C. Bossard, et al., in *Crystal Engineering: From Molecules and Crystals to Materials*, D. Braga, F. Grepioni, Eds. (Kluwer, Dordrecht, Netherlands, 1991), pp. 251–268.
6. M. C. Etter, K. S. Huang, *Chem. Mater.* **4**, 824 (1992).
7. M. S. Wong, V. Gramlich, C. Bosshard, P. Günter, *J. Mater. Chem.* **7**, 2021 (1997).
8. W. Lin, O. R. Evans, R.-G. Xiong, Z. Wang, *J. Am. Chem. Soc.* **120**, 13272 (1998).
9. S. R. Marder, J. W. Perry, W. P. Schaefer, *Science* **245**, 626 (1989).

10. S. R. Marder, J. W. Perry, W. P. Schaefer, C. P. Yakymyshyn, *Chem. Mater.* **6**, 1137 (1994).
11. W. Tam et al., *Chem. Mater.* **1**, 128 (1989).
12. O. König, H.-B. Burgi, Th. Armbruster, J. Hulliger, Th. Weber, *J. Am. Chem. Soc.* **119**, 10632 (1997).
13. V. A. Russell, C. C. Evans, W. Li, M. D. Ward, *Science* **276**, 575 (1997).
14. K. T. Holman, M. D. Ward, *Angew. Chem. Int. Ed.* **39**, 1653 (2000).
15. J. A. Swift, A. M. Pivovar, A. M. Reynolds, M. D. Ward, *J. Am. Chem. Soc.* **120**, 5887 (1998).
16. V. A. Russell, M. C. Etter, M. D. Ward, *J. Am. Chem. Soc.* **116**, 1941 (1994).
17. K. T. Holman, A. M. Pivovar, J. A. Swift, M. D. Ward, *Acc. Chem. Res.* **34**, 107 (2001).
18. K. T. Holman, S. M. Martin, D. P. Parker, M. D. Ward, *J. Am. Chem. Soc.* **123**, 4421 (2001).
19. J. A. Swift, M. D. Ward, *Chem. Mater.* **12**, 1501 (2000).
20. The term banana-shaped has also been used to describe thermotropic liquid crystal compounds [G. Petzl, S. Diele, W. Weissflog, *Adv. Mater.* **11**, 707 (1999)].
21. According to the defined axes *a*, *b*, and *c* in Fig. 2, the space group assignment must strictly be *Im2m*. For clarity, however, the discussion adopts the standard crystallographic notation of *Im2* for this space group, with the understanding that the notations are related by a simple transformation of the *b* and *c* axes. The *I*-centering condition is enforced by the connectivity of the pillars and sheets, with adjacent sheets being offset along the *a* axis by exactly *a*/2.
22. The strategy used here based on GS inclusion compounds constructed from banana-shaped pillars is not related to the factors that govern polar ordering in crystals of meta-disubstituted benzenes, which crystallize more often in polar space groups than do their para- or ortho-substituted derivatives because of simple packing considerations [L. S. Rez, *Kristallographie* **5**, 63 (1960) and A. C. Skrapski, *J. Chem. Soc. Perkin Trans. 2*, 1197 (1973)].
23. Strictly speaking, the MDS and TMBDS pillars do not possess perfect C_{2v} symmetry, owing to the reduction of symmetry by the methyl hydrogens (in the

absence of free rotation of the methyl group) and steric forces that cause minute out-of-plane distortions of the substituents [A. Koeberg-Telder, H. Cerfontain, C. H. Stam, G. Kreuning, *Recl. Trav. Chim. Pays-Bas* **106**, 142 (1987); M. A. M. Meester, H. Schenk, *Recl. Trav. Chim. Pas-Bas* **91**, 213 (1972)].

24. D. S. Chemla, J. Zyss, *Nonlinear Optical Properties of Organic Molecules and Crystals*, vol. 1 and 2 (Academic Press, Orlando, FL, 1987).
25. *Nonlinear Optical Effects and Materials*, P. Gunter, Ed. (Springer Series in Optical Sciences, vol. 72, Berlin, Germany, 2000).
26. J. Zyss, J. L. Oudar, *Phys. Rev. A* **26**, 2028 (1982).
27. The lattice parameters *a*, *b*, and *c* depicted in Fig. 2 represent orthogonal vectors that are strictly appropriate only for host frameworks with orthorhombic symmetry. The near-*Im2* frameworks are a consequence of slight deviations of the *a*, *b*, and/or *c* axes from orthogonality, with concomitant losses of one or more mirror planes, C_2 , and/or screw axes because of the fixed guest orientations. The real lattice parameters of these lower symmetry frameworks have been transformed to the orthorhombic convention for convenient comparison in Table 1.
28. Though we have not observed any inclusion compounds with 1,3-benzene- and 2,4-dimethyl-1,5-benzenedisulfonates, other GS host framework architectures are possible with banana-shaped pillars. For example, double-brick architectures have been observed in G_2MDS and G_2MDBDS with guests other than those described here (18).
29. S. K. Kurtz, T. T. Perry, *J. Appl. Phys.* **39**, 3798 (1968).
30. M. E. Brown, J. D. Chaney, B. D. Santarsiero, M. D. Hollingsworth, *Chem. Mater.* **8**, 1588 (1996).
31. Supported in part by the Materials Research Science and Engineering Center program of NSF under award number DMR-9809364 and the NSF Division of Materials Research (DMR-9908627). K.T.H. gratefully acknowledges a postdoctoral fellowship from Natural Sciences and Engineering Research Council of Canada. We also thank V. Young Jr. for crystallographic assistance.

16 July 2001; accepted 1 November 2001

Seismic Detection of Rigid Zones at the Top of the Core

Sebastian Rost* and Justin Revenaugh

Data from earthquakes in the Tonga-Fiji region recorded at a seismic array in northern Australia show evidence for rigid zones at the top of the outer core. The *ScP* waveforms can be modeled by thin (0.12 to 0.18 kilometer) zones of molten iron mixed with solid material with a small, but positive, *S*-wave velocity (0.6 to 0.8 kilometer per second) that enables the propagation of *S*-waves in the outermost core. The zones may be topographic highs of the core-mantle boundary filled by light core sediments and might be important for variation of Earth's nutation and for convection of the outer core.

The core-mantle boundary (CMB) region, where the molten iron outer core meets the solid silicate mantle, represents the largest compositional and rheological contrast in Earth's interior. Strong lateral variations of *S*- and *P*-wave velocity exist in the lowermost 200 to 300 kilometers of the mantle above the CMB (1–4), a region capped in

many places by a sharp discontinuity (5, 6). In the lowermost few tens of kilometers of the mantle, ultralow-velocity zones (ULVZ) have been detected (7–9) and interpreted as evidence for partial melt or chemical contamination of the lowermost mantle by the outer core (10–12). Both explanations have significant implications for core and mantle dynamics (13–16). ULVZ are discussed as source regions of mantle plumes and may control the frequency of Earth's magnetic field reversals (17, 18). Recently, models of the CMB with

Department of Earth Sciences, University of California, Santa Cruz, CA 95064, USA.

*To whom correspondence should be addressed. E-mail: srost@es.ucsc.edu

REPORTS

a thin metallic rigid layer at the top of the core have been shown to fit some anomalous diffracted *SKS* waves and the nutation of Earth's rotation (12, 19). If shown to be necessary, these zones would extend CMB heterogeneity into the core.

We studied *ScP* phases (a shear wave that is converted to a compressional wave upon reflection from the CMB) to resolve the fine-scale structure of the CMB (20–22). We used earthquakes from the Tonga-Fiji subduction zone recorded at the small-aperture, short-period Warramunga array (WRA) in the Northern Territories of Australia (Fig. 1). The data set consists of 83 events with depths ≥ 300 km, distances of $\Delta = 40^\circ$ to 44° , and body wave magnitudes of $m_b = 4.3$ to 6.0. Array data allowed us to calculate receiver stacks (23) and model waveforms of individual events, increasing the spatial resolution of elasticity and density variations.

Most of the events studied show either the simple *ScP* waveforms predicted by global-average spherical Earth models (e.g., IASP91) or evidence for ULVZ structure above the CMB, but seven events from three different regions (Fig. 2A) showed complex waveforms (Fig. 2B) characterized by a second large arrival after *ScP* that cannot be modeled with IASP91 or an ULVZ structure. The ULVZ can produce large coda phases (24), but not with amplitudes as large as or larger than *ScP* as observed here. Waveform modeling with the Gaussian-Beam method (GBM) (25, 26) was used to calculate synthetic seismograms for IASP91 with an ULVZ and/or core rigidity zone (CRZ) at the CMB. We used an explosion line source and convolved the calculated seismograms with the array summed *P*-wavelet of the event. Modeling of the unusual waveforms (Fig. 2B) included a thin ULVZ of several kilometers thickness, velocity reductions of 0 to 15% and 0 to 30% for *P*- and *S*-waves, respectively, and density increases of 0 to 50%, but could not explain the primary characteristics of the data, especially the large second onset. Modeling of the CRZ included thicknesses of up to 2 km, *S*-wave velocities of up to 5.5 km/s, and density reductions of up to 40%. The synthetic waveforms replicate all major features of the data (Fig. 2B). The largest of the additional phases that contribute to the complex *ScP* waveforms is the conversion of the CRZ *S*-wave into a *P*-wave at the CMB upon exiting the core (*Sc*spP*) (Fig. 3). Models that fit the data best have CRZ thicknesses of ~ 150 m, *S*-wave velocities of 0.6 to 0.8 km/s, and a density reduction of 10 to 40% relative to the outermost core in IASP91 and PREM (27, 28). Because the dominant phases travel as *S*-waves through the CRZ, a change of the *P*-wave velocity has little effect. A trade-off exists between CRZ thickness and *S*-wave velocity, because the model parameters (thickness, v_s , ρ) outnumber the constraints

(*Sc*spP*-to-*ScP* amplitude ratio and time separation), but thicknesses greater than 1.2 km cannot fit the data with plausible density structures. The waveform fit of these thicker models is generally worse. The modeled CRZs are very thin. We are able to resolve them because the slow *S*-wave velocities in the CRZ result in travel time differences large enough to separate *ScP* and *Sc*spP* (Fig. 4). High CRZ *S*-wave velocities produce high *Sc*spP*-to-*ScP* amplitude ratios, whereas decreased density relative to normal core material reduces postcursor amplitudes. The main waveform characteristics of the data are explained by CRZs that would also affect *PcS* but not *PcP*. The addition of ULVZs alters the waveforms by appending pre- and postcursors that improve the fit slightly at the beginning or the end of the wavelet [supplemental fig. 1 (29)].

We modeled one-dimensional (1D) velocity structures only. Our results indicate that the lower mantle in this region contains three-dimensional (3D) velocity structure, and 1D modeling is an oversimplification, but one we believe is justified given the excellent waveform matches obtained and the lack of high-frequency 3D modeling codes.

We controlled the slowness and backazimuth of *ScP* with an *fk*-analysis (30). All phases arrive, within the resolution of the array, along the theoretical backazimuth and with the correct slowness. Because of the short time gaps between *ScP* and its postcursors, a scattered-wave origin cannot be ruled out. However, the different events show similar waveforms and travel time differences between the *ScP* and *Sc*spP* wavelets. A scattering origin would require similar small-scale structure at the different conversion points, which is unlikely. Another possibility is that multipathing within the slab produces complicated *ScP* waveforms. With the subducting slab configuration in Tonga-Fiji, *ScP* leaves the slab quickly. The *P*-phase travels further within the slab and is more likely to have a complicated waveform. The similarity of *P*-waveforms for events whose locations and foci vary by ~ 150 km argues against pervasive slab multipathing.

A major tool used to probe the CMB is diffracted *SKS* waves [*SP_dKS*; e.g., (31)]. Anomalous *SP_dKS* can be explained by ULVZ or CRZ (19, 32). ULVZ structure alone cannot explain our data (Fig. 4). CRZ structure in agreement with *SP_dKS* data show

Fig. 1. Source receiver combination used for this study. Earthquakes are marked by small gray circles and are located in the southern Tonga-Fiji region. They are recorded at the short-period, small-aperture Warramunga array (WRA) in the Northern Territories of Australia (triangle). The array consists of 20 vertical-component, short-period (1 Hz) stations with an interstation spacing of ~ 2.5 km (see inset). The ellipse marks the approximate conversion zone of the *ScP* waves at the CMB. Thin lines are suggested plate boundaries (41).

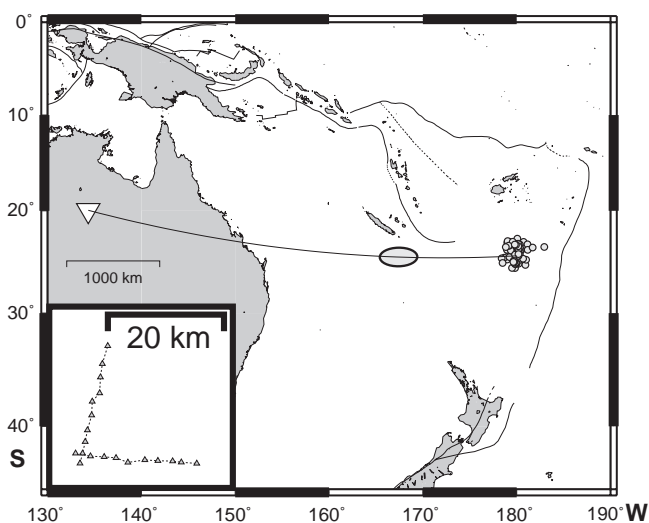


Table 1. Events showing CRZ structure. Lat., latitude; Lon., longitude; Θ , backazimuth.

Event no.	Origin	Lat. ($^\circ$)	Lon. ($^\circ$)	Depth (km)	m_b	Δ ($^\circ$)	Θ ($^\circ$)
1	06 January 1980 22:10	-23.80	-179.81	506	5.0	42.58	103.78
2	20 May 1980 04:24	-23.78	-179.80	539	5.2	42.59	103.75
3	20 November 1979 19:28	-23.82	-179.76	518	5.0	42.63	103.81
4	21 February 1982 14:18	-23.87	-179.73	515	5.0	42.65	103.89
5	18 July 1984 06:01	-23.89	-179.60	534	4.9	42.77	103.93
6*	03 July 1979 02:50	-23.92	-179.49	456	5.0	42.87	103.98
7*	21 February 1985 06:56	-23.91	-179.78	531	5.1	42.60	103.94
8†	24 November 1979 06:10	-24.68	178.67	589	5.1	41.15	104.97
9†	10 September 1979 07:38	-25.70	179.82	472	5.2	42.15	106.56
10†	11 September 1980 10:30	-25.69	179.50	492	4.9	41.86	106.53

*Events show complex waveforms that can be modeled as CRZ or extreme ULVZ.

†Events are located in different regions.

REPORTS

maximum velocities of 8 and 3 km/s for *P*- and *S*-waves, respectively, densities of about 9.6 g/cm³, and thicknesses of 1 to 2 km (12, 19, 32). These maximum models cannot explain the anomalous waveforms in our data set: the predicted differential travel times and postcursor amplitudes are too large, although the *S*-wave velocity found here is in the range given by (19).

The CRZs documented in this study cover a small area of the CMB with simple *ScP* waveforms consistent with IASP91 close by, indicating changes of CMB structure over lateral scales of a few tens of kilometers. However, the CRZ thicknesses are close to the detection threshold of our data. CRZs thinner than ~0.1 km may not be detected in the *ScP* waveforms. Different models for finite rigidity at the top of Earth's core have

been discussed. High-pressure experiments document reaction of (Fe,Mg) SiO₃ perovskite with liquid iron from the outer core at CMB conditions, forming FeO and FeSi alloys (10, 33, 34). However, it appears unlikely that this process can produce a layer thicker than a few meters (35), and we will not discuss it further.

A second group of models propose sediments at the top of the core to explain seismic and geodetic observations (19, 36). The core is composed of Fe and Ni and one or more lighter alloying components (37). The lighter components in the core may be saturated due to exchange with the mantle (19). Cooling and solidification of the inner core disturbs the equilibrium by enriching the light component in the outer core. Chemical equilibrium is maintained by precipitation of lighter compo-

nent-bearing solid phases, forming a mushy layer of a solid matrix interspersed with liquid Fe (19) in topographic highs of the CMB that offer protection from the fast convection currents of the outer core. The root-mean-square amplitude of the global CMB topography is ~350 m (38, 39), similar to the CRZ thicknesses we infer. Pure FeO and FeSi, two components possibly forming the CRZ (19), are ~50% less dense than core material, requiring a mixture of solid Fe alloys and liquid Fe in the CRZ to fit our data. Liquid Fe, however, should drain out of the layer due to its higher density. A mixture could be produced by vigorous convective mixing of the uppermost outer core or be a transient state due to sediment compaction.

Several *ScP* waveforms indicate the existence of ULVZs in addition to CRZs [supplemental fig. 1 (29)]. Some ULVZ models propose partial melting as the source of the velocity reductions (11). A partially molten

Fig. 2. (A) Detailed event location map. The ellipse outlines the central region where CRZ waveforms are observed (except for 13). Event hypocenters vary by ~150 km laterally and in depth. Events marked by an asterisk show complicated *P*-waveforms and are not modeled, because the comparison with the modeled waveform is ambiguous. **(B)** Data showing *ScP* requiring CRZ structure (events 1 through 7). Shown are hand-aligned and linearly summed traces of the array. To reduce noise, the traces are filtered with a second-order Butterworth bandpass filter with cut-off frequencies of 0.5 and 1.6 Hz. The CRZ structure in this region of the CMB produces additional large postcursors to *ScP*, as marked by the arrows in the blue data traces. The underlying red trace shows the synthetic waveform best fitting the data. The *P*-wavelet (green trace) is shown for comparison. Event numbering refers to (A). Events 8 through 16 have simple *ScP* waveforms, presumably converted at a simple CMB. These events lie mostly to the west of the CRZ region. Note the similarity of the *P*- and *ScP*-wavelet for most events.

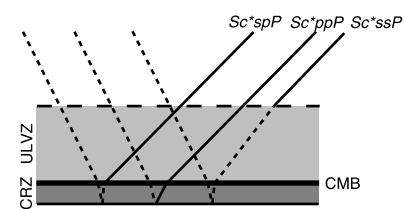
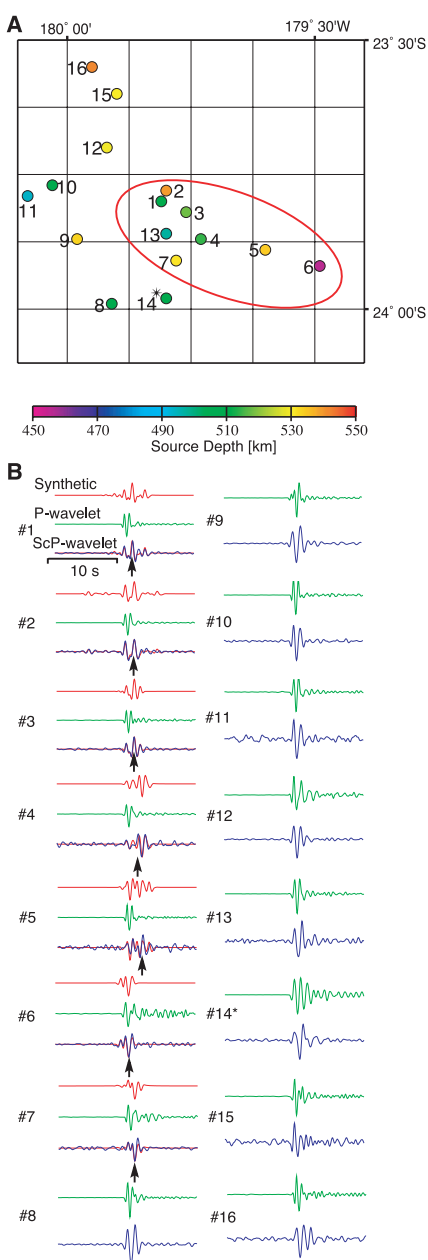


Fig. 3. Paths of some of the energetic phases generated by CRZ (a CRZ only produces postcursors to *ScP*). The reflection at the bottom of the CRZ is denoted by *c**. The highest amplitude secondary arrival is the *S*→*P* conversion of the ascending branch (*Sc***spP*). Higher-order reverberations occur but are smaller in amplitude and more strongly damped by high attenuation within the CRZ.

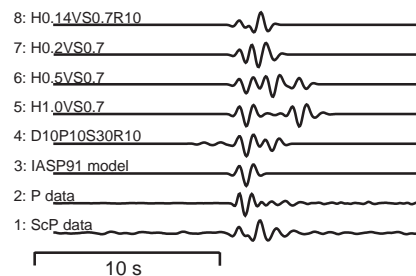


Fig. 4. Synthetic seismograms and data for different CRZ models. The bottom traces show the *ScP*- and *P*-wavelets for event 1 (Table 1). Trace 3 shows the predicted *ScP* wavelet for an IASP91 CMB (27), i.e., a first-order discontinuity. A synthetic seismogram for a 10-km-thick ULVZ with -10% *V_p* and -30% *V_s* change and 10% density increase is shown in trace 4. The wavelet shows pre- and postcursors not visible in trace 3. Traces 5 through 7 show CRZ models with different thicknesses: 1, 0.5, and 0.2 km, respectively. *V_s* for all these models is 0.7 km/s. The top trace 8 shows a synthetic for a 0.14-km-thick CRZ with *V_s* = 0.7 km/s and a 10% density decrease relative to the core material, which best fits the data.

layer in contact with the molten iron of the core would enhance the chemical reactions (40), releasing additional Si and O and explaining a possible affinity of CRZs with ULVZs.

References and Notes

1. E. J. Garnero, *Annu. Rev. Earth Planet. Sci.* **28**, 509 (2000).
2. K. E. Bullen, *Mon. Not. R. Astron. Soc. Geophys. Suppl.* **5**, 355 (1949).
3. S. Grand, *J. Geophys. Res.* **99**, 11591 (1994).
4. W.-J. Su, R. L. Woodward, A. M. Dziewonski, *J. Geophys. Res.* **99**, 6945 (1994).
5. T. Lay, D. V. Helmberger, *Geophys. J. R. Astron. Soc.* **75**, 799 (1983).
6. M. H. Weber, *Geophys. J. Int.* **115**, 183 (1993).
7. E. J. Garnero, D. V. Helmberger, *Geophys. Res. Lett.* **23**, 977 (1996).
8. J. Revenaugh, R. Meyer, *Science* **277**, 670 (1997).
9. E. J. Garnero, J. Revenaugh, Q. Williams, T. Lay, L. H. Kellogg, in *The Core-Mantle Boundary Region*, M. Gurnis, M. E. Wysession, E. Knittle, B. Buffett, Eds., vol. 28 of *Geodynamics* (American Geophysical Union, Washington, DC, 1998), pp. 319–334.
10. M. Manga, R. Jeanloz, *Geophys. Res. Lett.* **23**, 3091 (1996).
11. Q. Williams, E. J. Garnero, *Science* **273**, 1528 (1996).
12. E. J. Garnero, R. Jeanloz, *Geophys. Res. Lett.* **27**, 2777 (2000).
13. E. Knittle, R. Jeanloz, *Geophys. Res. Lett.* **15**, 609 (1989).
14. ———, *Science* **251**, 1438 (1991).
15. B. A. Buffett, *Geophys. J. Int.* **125**, 303 (1996).
16. N. L. Montague, L. H. Kellogg, M. Manga, *Geophys. Res. Lett.* **25**, 2345 (1998).
17. Q. Williams, J. Revenaugh, E. Garnero, *Science* **281**, 546 (1998).
18. G. A. Glatzmeier, R. S. Coe, L. Hongre, P. H. Roberts, *Nature* **401**, 885 (1999).
19. B. A. Buffett, E. J. Garnero, R. Jeanloz, *Science* **290**, 1338 (2000).
20. E. J. Garnero, J. E. Vidale, *Geophys. Res. Lett.* **26**, 377 (1999).
21. C. Reasoner, J. Revenaugh, *J. Geophys. Res.* **105**, 28173 (2000).
22. S. E. Persh, J. E. Vidale, P. S. Earle, *Geophys. Res. Lett.* **28**, 387 (2001).
23. Receiver stacks or slant stacks account for the time offset between the individual array recordings due to different incident angles of the wavefront at the array prior to summation of traces. Incoherent noise and coherent phases with deviating incidence angles are suppressed, whereas the phase of interest is amplified.
24. J. C. Castle, R. D. van der Hilst, *Earth Planet. Sci. Lett.* **176**, 311 (2000).
25. M. H. Weber, *Geophys. J. Int.* **92**, 9 (1988).
26. GBM synthetics were compared with computationally intensive reflectivity synthetics [G. Müller, *J. Geophys. Res.* **58**, 153 (1985)] to ensure their accuracy.
27. B. L. N. Kennett, E. R. Engdahl, *Geophys. J. Int.* **105**, 429 (1991).
28. A. M. Dziewonski, D. L. Anderson, *Phys. Earth Planet. Inter.* **25**, 297 (1981).
29. Supplemental material is available at Science Online at www.sciencemag.org/cgi/content/full/294/5548/1911/DC1
30. H.-P. Harjes, M. Henger, *Z. Geophys.* **39**, 865 (1973).
31. E. J. Garnero, D. V. Helmberger, *Phys. Earth Planet. Inter.* **91**, 161 (1995).
32. E. J. Garnero, R. Jeanloz, *Science* **289**, 70 (2000).
33. E. Knittle, R. Jeanloz, *J. Geophys. Res.* **96**, 16169 (1991).
34. X. Song, T. J. Ahrens, *Geophys. Res. Lett.* **21**, 153 (1994).
35. J. P. Poirier, V. Malavergne, J. L. LeMouél, in (9), pp. 131–137.
36. S. I. Braginsky, *Phys. Earth Planet. Inter.* **111**, 21 (1999).
37. F. Birch, *J. Geophys. Res.* **69**, 4377 (1964).
38. P. S. Earle, P. M. Shearer, *Science* **277**, 667 (1997).

39. P. M. Shearer, M. A. H. Hedlin, P. S. Earle, in (9), pp. 37–56.
40. E. Ito, K. Morooka, O. Ujike, T. Kasura, *J. Geophys. Res.* **100**, 5901 (1995).
41. O. Gudmundsson, M. Sambridge, *J. Geophys. Res.* **103**, 7121 (1998).

42. We thank G. Jahnke, C. Wicks, and M. Richards for the WRA data set. G. Glatzmeier and Q. Williams provided helpful comments. Supported by NSF Geophysics and CSED1.

22 August 2001; accepted 25 October 2001

Detection of Molecular Hydrogen in the Atmosphere of Mars

Vladimir A. Krasnopolsky^{1*} and Paul D. Feldman²

Four hydrogen (H₂) lines have been detected in a spectrum of Mars observed with the Far Ultraviolet Spectroscopic Explorer. Three of those lines are excited by the solar Lyman β photons. The line intensities correspond to a column H₂ abundance of 1.17 (±0.13) × 10¹³ per square centimeter above 140 kilometers on Mars. A photochemical model for the upper atmosphere that simulates the observed H₂ abundance results in an H₂ mixing ratio of 15 ± 5 parts per million in the lower atmosphere. The H₂ and HD mixing ratios agree with photochemical fractionation of D (deuterium) between H₂O and H₂. Analysis of D fractionation among a few reservoirs of ice, water vapor, and molecular hydrogen on Mars implies that a global ocean more than 30 meters deep was lost since the end of hydrodynamic escape. Only 4% of the initially accreted water remained on the planet at the end of hydrodynamic escape, and initially Mars could have had even more water (as a proportion of mass) than Earth.

Mars' atmosphere has a total pressure of 6 mbar and consists of CO₂ (95.5%), N₂ (2.7%), H₂O [variable amounts, ~150 parts per million (ppm)], products of their photochemistry, and noble gases. Among the photochemical products, CO (0.07%), O, O₂ (0.13%), O₃, H, and NO have been detected (1, 2). Photochemical models of the martian atmosphere (3, 4) predict a comparatively high (~40 ppm) mixing ratio of H₂.

Despite the low abundance of water vapor in the atmosphere, its dissociation and the subsequent chemistry of the photolysis products play a crucial role in preventing the accumulation of CO and O₂ and therefore supporting the stability of CO₂. Molecular hydrogen forms in Mars' middle atmosphere at 20 to 50 km by the reaction between H and HO₂. H₂ is delivered to the upper atmosphere as a result of atmospheric mixing and diffusion. Decomposition of H₂ to atomic hydrogen by ionospheric processes determines the extent of escape of hydrogen to space and therefore the extent of loss of water from Mars. Although the predicted H₂ mixing ratio is comparatively high, molecular hydrogen was not detected by spacecraft that visited Mars (5–7). We observed Mars using the Far Ultraviolet Spectroscopic Explorer (FUSE) to

detect and measure H₂ in Mars' upper atmosphere.

FUSE consists of four co-aligned telescopes that cover a range of 904 to 1186 Å (8). Each telescope has a diffraction grating and a focal plane assembly with four apertures, and shares two segments at one of two detectors. This results in eight spectra per orbit for each aperture. The spectra consist of 16,384 pixels of ~6.5 mÅ each.

We observed Mars on 12 May 2001, when the heliocentric and geocentric distances of Mars were 1.512 and 0.58 AU (9), respectively, with angular diameter = 16.2 arc sec, phase (Sun-Mars-Earth) angle = 24°, solar longitude $L_S = 160^\circ$, geocentric velocity = -10.4 km s⁻¹, and solar activity index $F_{10.7\text{ cm}} = 140$. Solar longitude is used to specify seasons on Mars, and $L_S = 160^\circ$ corresponds to 2 September in the terrestrial calendar. The exospheric temperature was $T_\infty = 270\text{ K}$ (10) for the season and solar activity index during the observation. The observation was made in six FUSE orbits with a total exposure of 5 hours.

The instrument resolving power is $\lambda/\delta\lambda = 24,000$ for point sources and 5000 for Mars, which was observed with the 30 × 30 arc sec aperture. The spectral line width is 0.2 Å for this resolving power. Another aperture was used to control the terrestrial airglow foreground, which was very weak at the FUSE altitude of 768 km. We summed 96 observed spectra to obtain composite spectra of Mars and the foreground (11). These composite

¹Department of Physics, Catholic University of America, Washington, DC 20064, USA. ²Department of Physics and Astronomy, Johns Hopkins University, Baltimore, MD 21218, USA.

*To whom correspondence should be addressed. E-mail: vkran@altavista.com